EARTHARXIV PREPRINT COVERSHEET

Rapid Source Constraints and Nodal-Plane-Robust Static Stress Transfer of the 24 September 2026 Mw 5.3–5.4 Şanlıurfa Earthquake, Southeastern Türkiye

Shaheen Mohammed Saleh Ahmed

Department of Applied Geology, College of Science, University of Kirkuk, Kirkuk 36001, Iraq

Corresponding email: shaheengeolo@gmail.com

ORCID: https://orcid.org/0000-0002-9289-128X

Journal status: Prepared for concurrent submission to The Seismic Record (Seismological Society of America); not yet submitted at the time this preprint PDF was prepared.

Manuscript type: Research article / rapid earthquake source and static-stress analysis

Conflict of interest: None declared

Version date: 24 September 2026

Keywords: Şanlıurfa earthquake; Hilvan; Karaköprü; focal mechanism; P-wave first motion; Coulomb failure stress; static stress transfer; rapid seismology

Suggested EarthArXiv subjects: Geophysics and Seismology; Tectonics and Structural Geology; Natural Hazards; Engineering Geology

Data and code: Raw waveform and catalog data remain with the public providers. The processed waveform selection, mechanism grids, Coulomb grids, notebooks, and figures are being prepared for persistent public archiving; insert the Zenodo DOI when available.

IMPORTANT: This preprint reports a provisional, underconstrained focal mechanism. The Coulomb-stress sectors are monitoring priorities, not predictions of the next earthquake.

Rapid Source Characterization and Static Stress Transfer of the 24 September 2026 Mw 5.3–5.4 Şanlıurfa (Karaköprü–Hilvan) Earthquake, Southeastern Türkiye

First-hours waveform analysis, uncertainty, 2-D/3-D Coulomb stress modelling, and monitoring priorities

Shaheen Mohammed Saleh Ahmed

Department of Applied Geology, College of Science, University of Kirkuk, Kirkuk 36001, Iraq

Corresponding author: Shaheen Mohammed Saleh Ahmed | shaheengeolo@gmail.com | ORCID: https://orcid.org/0000-0002-9289-128X

NON-PEER-REVIEWED PREPRINT SUBMITTED TO EARTHARXIV • VERSION 1 • 24 SEPTEMBER 2026

Rapid-response status and scope
This manuscript is a same-day/first-hours scientific analysis of event us6000tx9u. It does not claim publication priority over other studies that may appear subsequently.
The focal mechanism is provisional: five automatic/weighted P-wave polarities, a 207.7° azimuth gap, and 1,588 near-best mechanisms demonstrate substantial non-uniqueness.
Coulomb stress maps identify model-dependent monitoring priorities. They do not predict the location, time, or magnitude of a future earthquake.

Highlights

- ✓ Open FDSN waveform data were processed within hours of the Mw 5.3–5.4 southeastern Türkiye earthquake.
- ✓ A provisional P-first-motion solution gives NP1 = 118°/66°/−50° and NP2 = 233.9°/45.6°/−145.3°.
- ✓ The perfect five-polarity fit is not unique: the azimuth gap is 207.7° and 1,588 near-best solutions remain.
- ✓ Both nodal-plane Coulomb scenarios share compact positive-stress sectors 5–10 km east and west of the USGS epicenter.
- ✓ Named settlement centers remain far below the +0.01 MPa consensus threshold in this model; monitoring priority should remain near-source and fault-specific.
- ✓ Same-day USGS DYFI data recorded 8 community responses and community intensity V, adding a preliminary macroseismic constraint independent of the waveform-derived stress model.

Abstract

On 24 September 2026, a moderate earthquake occurred in southeastern Türkiye near the Hilvan–Karaköprü sector of Şanlıurfa Province. The U.S. Geological Survey (USGS) reported M 5.3 at 37.4736°N, 38.8612°E and 10 km depth, whereas the Disaster and Emergency Management Authority of Türkiye (AFAD) issued a rapid Mw 5.4 solution at a shallower and approximately 5.9 km displaced hypocenter. We present a rapid, reproducible first-hours source and static-stress analysis based on openly accessible waveform and station metadata. The downloaded study archive contains 32 MiniSEED waveform files, 199 SAC traces, 25 StationXML response files, and 25 station-geometry records within a 200 km acquisition radius. After response correction, P-arrival refinement, polarity quality control, and geographic deduplication, five weighted vertical-component first motions were retained. A transparent double-couple grid search yields a provisional oblique mechanism with nodal planes NP1 = 118°/66°/−50° and NP2 = 233.9°/45.6°/−145.3°. Although all five retained polarities are fit, the solution is demonstrably underconstrained: the maximum azimuth gap is 207.7° and 1,588 near-best solutions remain. Using an Okada elastic half-space, Mw 5.3 as a working moment-magnitude proxy, 3 MPa stress drop, effective friction 0.4, and a magnitude-scaled 6.36 × 3.18 km rectangular source with 0.173 m mean slip, we calculate alternative NP1 and NP2 Coulomb failure stress (ΔCFS) fields. After excluding the inner 5 km source-core region and retaining only cells where both nodal-plane scenarios exceed +0.01 MPa, two compact consensus-positive sectors emerge approximately 5–10 km west and east of the USGS epicenter. Each covers about 34 km² and reaches a conservative scenario-overlap maximum near +0.05 MPa. By contrast, modeled ΔCFS at the centers of Hilvan, Şanlıurfa, Siverek, Bozova, Kâhta, and Adıyaman is much smaller than +0.01 MPa. An early AFAD ML 2.4 aftershock plots in a negative ΔCFS area under the source-plane receiver assumption, emphasizing that static stress maps are strongly dependent on receiver-fault orientation, source geometry, and rapid-location uncertainty. The immediate scientific priority is therefore dense near-source seismic monitoring, rapid relocation, regional moment-tensor inversion, InSAR/GNSS analysis, and fault-specific receiver-plane modelling—not deterministic prediction of the next earthquake. Same-day U.S. Geological Survey Did You Feel It? (DYFI) reporting had reached 8 community responses and community intensity V, providing preliminary evidence of moderate felt shaking but insufficient sampling for a stable spatial intensity-attenuation analysis.

Keywords

Şanlıurfa earthquake; Hilvan; Karaköprü; focal mechanism; P-wave first motion; Coulomb failure stress; static stress transfer; Atatürk Reservoir; East Anatolian tectonics; rapid earthquake response

1. Introduction

The Arabia–Anatolia collision zone is among the most actively deforming continental regions on Earth. GPS observations document north-northwestward motion of Arabia relative to Eurasia and westward escape/rotation of Anatolia, with a major component accommodated by the East Anatolian Fault (EAF) and distributed deformation in eastern and southeastern Türkiye (McClusky et al., 2000; Reilinger et al., 2006). The EAF is a ~700 km left-lateral plate-boundary fault with marked along-strike variations in slip rate, locking, seismicity, and focal-mechanism style (Güvercin et al., 2022). Its mapped geometry includes multiple segments, splays and stepovers, and the broader southeastern Anatolian region contains additional active fault systems that are not simply continuations of the principal EAF trace (Duman and Emre, 2013).

The 24 September 2026 earthquake occurred south of the principal EAF in a structurally complex part of Şanlıurfa Province that is also influenced by the local fault network around the Atatürk Reservoir. Previous work in this area identified the Bozova, Samsat, Kalecik and Lice faults and documented shallow moderate earthquakes near the reservoir, including damaging Mw 5.5 and Mw 5.1 events in 2017 and 2018 (Büyükakpınar et al., 2021). That study further demonstrated that tectonic stress, reservoir loading and pore-pressure diffusion may interact over multiyear timescales. Such a background makes rapid source characterization important, while also requiring caution against prematurely assigning a new earthquake to a particular mapped structure or anthropogenic process.

Static Coulomb stress modelling is widely used to investigate how a source rupture changes shear and normal stresses on surrounding receiver faults (King et al., 1994; Toda et al., 2005, 2011). The method is physically transparent but conditional: the calculated sign and amplitude depend on source geometry, slip distribution, receiver orientation, elastic structure, pore-pressure assumptions and hypocentral location. Rapid post-earthquake stress maps are therefore most useful as hypothesis-generating tools for prioritizing observations, not as deterministic forecasts.

This study provides a same-day rapid-response analysis of the 24 September 2026 earthquake using downloaded three-component waveforms, StationXML metadata, P-wave first-motion constraints, and alternative Coulomb stress scenarios. The goals are to (1) document the rapid agency solutions and waveform dataset; (2) derive and explicitly quantify the uncertainty of a provisional double-couple mechanism; (3) compute 2-D and 3-D static stress changes for both nodal planes; (4) identify stress-transfer features that are robust to nodal-plane ambiguity; and (5) translate those features into defensible monitoring priorities for subsequent field, seismic and geodetic investigations.

2. Regional tectonic and seismological setting

At regional scale, the northward motion of Arabia and the westward motion of Anatolia create a complex deformation field between the Dead Sea Fault, East Anatolian Fault, Anatolian interior and the Bitlis–Zagros collision zone. GPS solutions place an upper bound of roughly 9 ± 1 mm yr^{-1} on left-lateral slip along the EAF in earlier geodetic models, while later regional block models show substantial spatial variability in plate-boundary deformation (McClusky et al., 2000; Reilinger et al., 2006). Seismicity and moment-tensor studies confirm strong segmentation and local variations in the regional stress field (Güvercin et al., 2022).

The 2020 Mw 6.8 Sivrice earthquake demonstrated the importance of incomplete rupture and heterogeneous coupling along the EAF. Integrated strong-motion, GNSS, InSAR and teleseismic analyses showed that only part of the longer Sivrice–Pütürge segment ruptured, underscoring that mapped segment length and coseismic rupture length can differ substantially (Cheloni and Akinci, 2020; Konca et al., 2021). More recently, analyses of the 2023 Kahramanmaraş sequence have emphasized that both inherited stress and coseismic stress transfer can influence multi-fault rupture evolution (Nalbant et al., 2026).

Closer to the 2026 epicentral area, the Atatürk Reservoir region contains NW–SE and NE–SW fault structures, including the Bozova, Samsat, Kalecik and Lice faults. Büyükakpınar et al. (2021) documented an increase in shallow seismicity after reservoir impoundment and modelled the competing effects of instantaneous water loading and delayed pore-pressure diffusion. The present event is not here classified as reservoir-triggered: doing so would require source relocation, fault identification, hydrological forcing and long-term background-rate tests. The reservoir literature is used only to establish that the local crust is tectonically active and structurally heterogeneous.

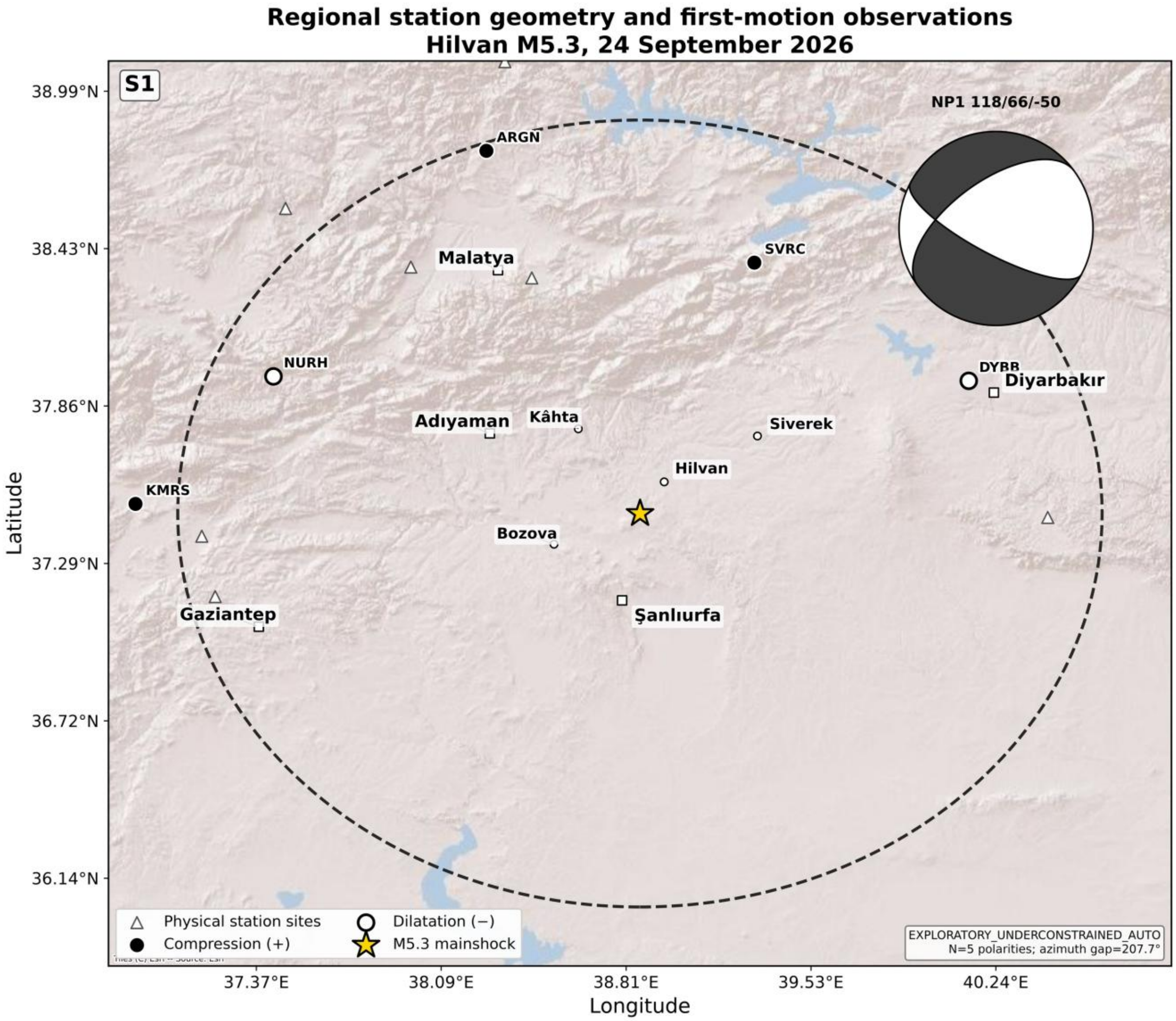

Figure 1. Regional geometry of the 24 September 2026 earthquake and the waveform stations used in the rapid analysis. The map includes the 200 km data-acquisition radius, physical station sites, the five retained first-motion observations, place names, and the provisional focal-mechanism inset. The status annotation in the original figure records that the focal solution is exploratory and underconstrained.

3. Event parameters and rapid-source dataset

3.1 Rapid agency solutions

Rapid earthquake parameters evolved during the first hours. The USGS solution used in the waveform workflow gives origin time 07:40:58 UTC, M 5.3, 37.4736°N, 38.8612°E and 10 km depth (event us6000tx9u). AFAD reported Mw 5.4 at approximately 07:40:56 UTC (10:40:56 Türkiye time), 37.4205°N, 38.86783°E and 7 km depth. The epicentral separation between these two rapid solutions is about 5.9 km. This offset is comparable to the radial distance of the strongest near-source Coulomb lobes identified later in this study and is therefore a first-order uncertainty, not a cosmetic catalogue difference.

Table 1. Rapid agency parameters for the 24 September 2026 earthquake.

Agency	Origin time	Magnitude	Lat. °N	Lon. °E	Depth km	Location label	Comment
USGS	07:40:58 UTC	5.3	37.4736	38.8612	10.0	15 km SSW of Hilvan	Primary waveform-model origin
AFAD rapid	07:40:56 UTC	Mw 5.4	37.4205	38.86783	7.0	Karaköprü	≈5.9 km from

						(Şanlıurfa)	USGS epicenter

Note: Rapid automatic/reviewed agency solutions may change as additional waveform and phase data are incorporated. The values above represent first-hours solutions used for sensitivity discussion.

3.2 Downloaded waveform archive

The study archive comprises 32 MiniSEED files, 199 SAC files, 25 StationXML response files and 25 station-geometry records. The actual acquisition radius recorded in the project metadata is 200 km. Original MiniSEED was preferred over duplicated SAC conversions when response metadata were available. Instrument responses were removed to velocity before polarity analysis, and vertical components were checked against metadata orientation. The workflow preferred HHZ/BHZ-type broadband channels and geographically deduplicated co-located observations.

P-wave travel times and takeoff angles were calculated with the iasp91 model (Kennett and Engdahl, 1991), followed by waveform-based P-onset refinement and first-motion quality control. Automatic polarity candidates were evaluated using signal-to-noise ratio, first-motion confidence and stability across more than one P-wave passband.

Figure 2. P-wave first-motion quality-control panel for selected vertical-component waveforms. Traces are response corrected and aligned on the refined P onset; the panel documents station distance, polarity, signal-to-noise ratio and confidence used in the rapid workflow.

3.3 USGS Did You Feel It? macroseismic observations

To complement the instrumental source analysis, the event was checked against the U.S. Geological Survey Did You Feel It? (DYFI) product on 24 September 2026. At the time of access, the USGS DYFI event listing for us6000tx9u showed 8 community responses and community intensity V. DYFI is a citizen-science product that aggregates questionnaire responses into community intensity information and is intended to supplement instrumental observations, especially where station coverage is limited.

DYFI field	Same-day status used in this manuscript
USGS event ID	us6000tx9u
Community responses	8
Displayed community intensity	V

Responses-versus-time product	Number of user responses accumulated as a function of time during the first 24 h after the event
Scientific use here	Independent preliminary macroseismic evidence of felt shaking
Important limitation	Sparse and evolving voluntary reports; not a stress-transfer or earthquake-forecast constraint

The responses-versus-time panel should be interpreted as the accumulation of voluntary internet reports, not as a seismogram, shaking-duration curve, or aftershock-rate series. USGS notes that DYFI products are preliminary and can change as new reports are submitted or quality-control procedures remove duplicated, misassociated, or otherwise unreliable entries. Because only eight responses were available during the same-day analysis window, no attempt is made here to fit an intensity prediction equation or infer detailed spatial site amplification from DYFI alone.

4. Methods

4.1 P-wave first-motion focal mechanism

First-motion focal mechanisms are sensitive to polarity errors, hypocentral uncertainty, takeoff-angle uncertainty and network geometry. The conceptual basis follows the double-couple radiation approach used in classical first-motion methods, while the uncertainty concerns are consistent with HASH/SKHASH methodology (Hardebeck and Shearer, 2002; Skoumal et al., 2024). The present rapid solution is intentionally transparent: candidate strike, dip and rake combinations were evaluated on a coarse 10° grid and refined locally at 2° spacing. For each candidate, the sign of the predicted P-wave radiation amplitude was compared with the observed polarity and weighted by polarity confidence.

Three polarities passed the strict automatic threshold (SVRC, DYBB and ARGN). Two additional observations (KMRS and NURH) were admitted as lower-weight fallback measurements to improve azimuthal coverage. These fallback observations were not treated as equally reliable: their weights were reduced relative to the strict picks. This distinction is crucial because a perfect polarity fit with only five observations can be highly non-unique.

Table 2. P-wave first-motion observations retained in the provisional focal-mechanism inversion.

Station	Ch.	Dist. km	Az. °	Takeoff °	Pol.	SNR	Conf.	Selection
KO.SVRC	HHZ	107.8	21.1	94.8	+	44.1	4.57	strict auto
KO.DYBB	HHZ	124.4	64.2	63.0	−	30.5	5.06	strict auto
KO.KMRS	HHZ	173.1	271.9	45.9	+	8.1	3.08	fallback auto for coverage
KO.NURH	HHZ	136.9	294.2	45.9	−	9.7	3.31	fallback auto for coverage
KO.ARGN	HHZ	154.0	340.3	45.9	+	25.6	5.21	strict auto

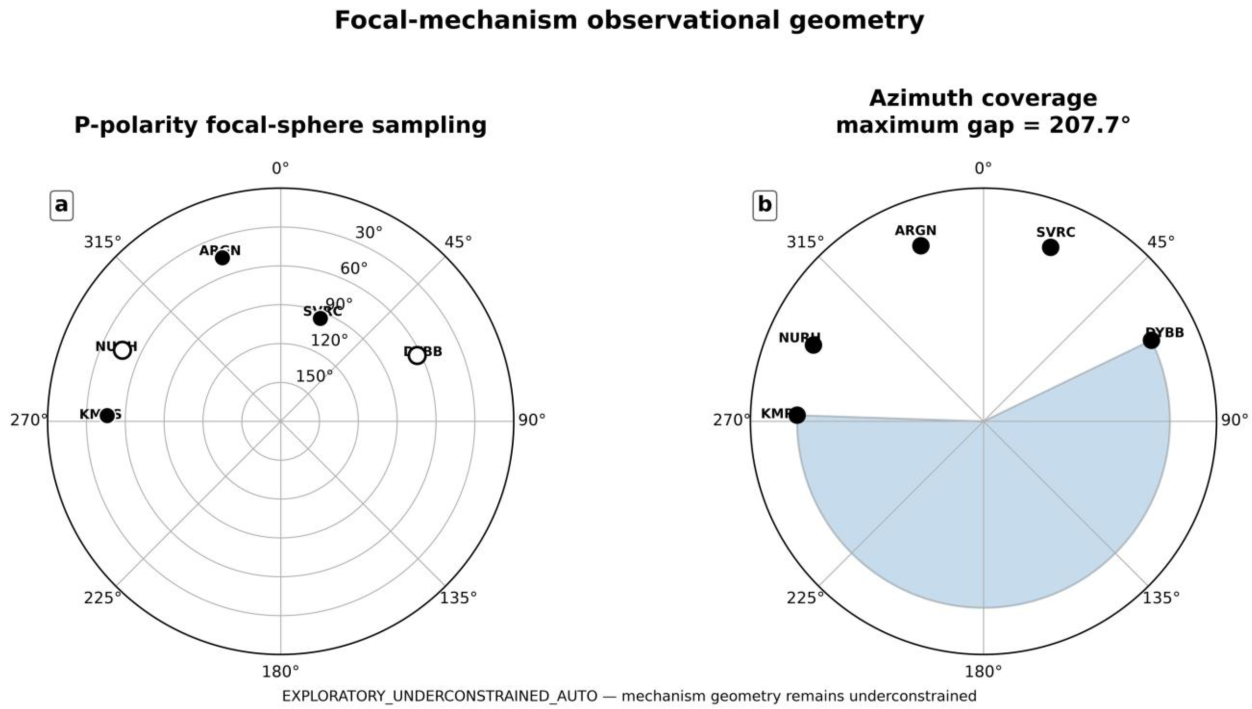

Figure 3. Focal-sphere sampling and azimuth coverage. The maximum azimuth gap is 207.7°, exceeding the usual 180° geometric screening criterion and demonstrating that the current focal mechanism is not well constrained.

4.2 Source scaling

Because no finite-fault or geodetic slip model was available within the rapid analysis window, the earthquake was represented by a uniform rectangular dislocation. Scalar seismic moment was estimated using $M0 = 10^{(1.5Mw + 9.1)}$ N m. An equivalent circular-crack radius was estimated from $r = [7M0/(16\Delta\sigma)]^{(1/3)}$, where $\Delta\sigma$ is stress drop. The circular area was converted to a 2:1 rectangle, and uniform slip D was calculated from $M0 = \mu AD$ using shear modulus $\mu = 32$ GPa. With $Mw = 5.3$ and $\Delta\sigma = 3$ MPa, the working source dimensions are 6.36 × 3.18 km and the mean slip is 0.173 m. These values are modelling assumptions rather than independent observations.

4.3 Static Coulomb failure stress

Static elastic displacements and stress changes were calculated using the Okada (1992) rectangular dislocation solution in a homogeneous isotropic half-space. The Coulomb failure stress change was resolved as $\Delta CFS = \Delta\tau + \mu'(\Delta\sigma n + \Delta P)$, where $\Delta\tau$ is shear-stress change in the receiver-slip direction, $\Delta\sigma n$ is normal-stress change under the workflow sign convention, μ' is effective friction, and ΔP is pore-pressure change. The rapid models set $\mu' = 0.4$ and $\Delta P = 0$. Source and receiver orientations were taken to be the same nodal plane in each alternative scenario. Thus NP1 and NP2 maps are alternative self-oriented receiver scenarios—not stress maps on every mapped fault in the region.

Following the stress-interaction literature, positive ΔCFS is interpreted as a modeled change that promotes failure on the specified receiver geometry and negative ΔCFS as a change that inhibits it (King et al., 1994; Toda et al., 2005). A +0.01 MPa (10 kPa, 0.1 bar) contour is used only as a convenient monitoring-screening reference. It is not a universal triggering threshold and is not converted into earthquake probability.

4.4 Nodal-plane-robust consensus metric

To reduce dependence on the unresolved nodal plane, we define a conservative consensus field $C(x,y) = \min[\Delta CFS\_NP1(x,y), \Delta CFS\_NP2(x,y)]$. A grid cell is designated a robust-positive monitoring cell only when both nodal-plane scenarios exceed +0.01 MPa. Cells within 5 km of the source center are excluded from this screening because a uniform finite rectangular source produces strong source-edge gradients and near-source values are especially sensitive to rupture placement, discretization and receiver assumptions. Connected-component analysis is then applied to the remaining consensus-positive cells.

5. Results

5.1 Provisional focal mechanism and non-uniqueness

The refined grid search returns NP1 = strike 118°, dip 66°, rake −50° and the auxiliary plane NP2 = strike 233.9°, dip 45.6°, rake −145.3°. All five retained polarities are reproduced by this mechanism, yielding zero weighted polarity misfit in the selected grid. Nevertheless, the solution should not be described as a uniquely resolved focal mechanism. The 207.7° azimuth gap means more than half of the focal sphere lacks independent azimuthal control, and 1,588 near-best mechanisms lie within the adopted misfit tolerance. The solution therefore indicates an oblique mechanism family but does not yet establish a definitive strike, dip, rake or physical rupture plane.

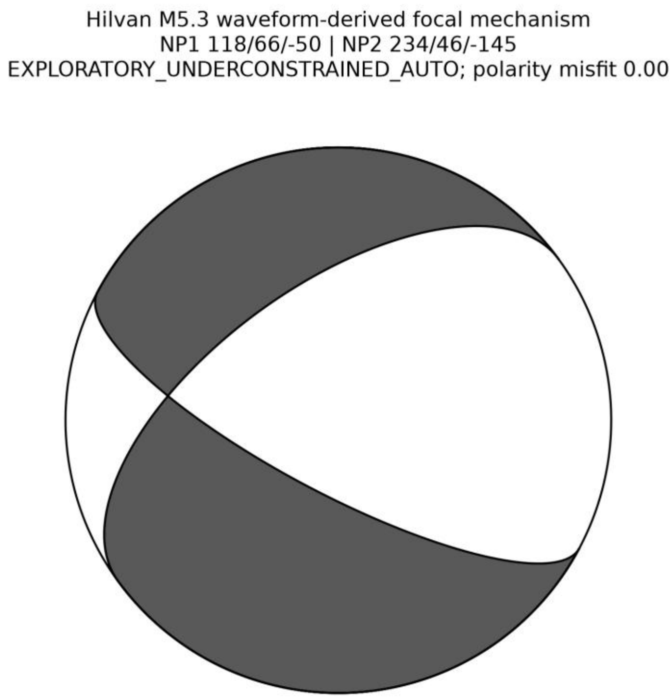

Figure 4. Provisional double-couple focal mechanism from the rapid first-motion inversion. The beachball is a preferred grid-search solution, not a unique mechanism.

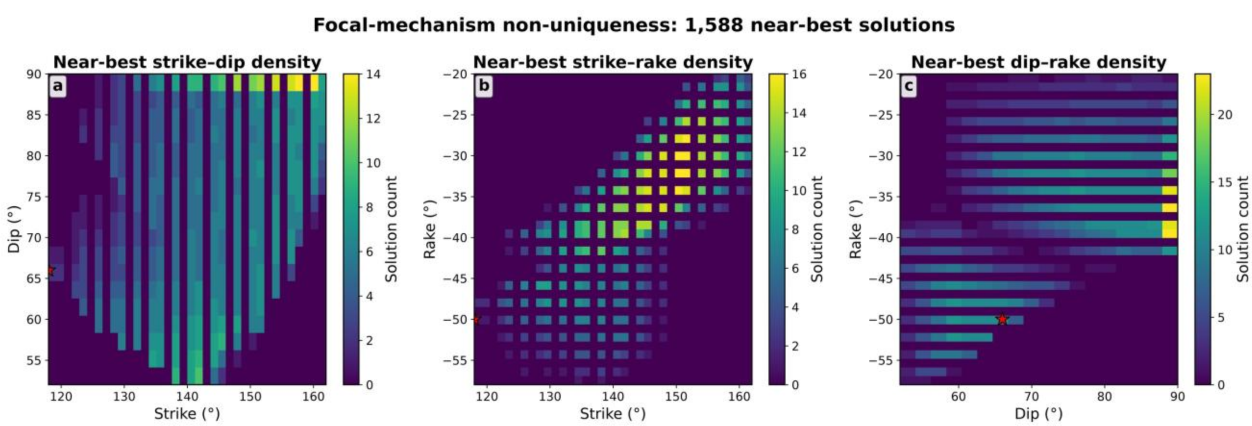

Figure 5. Density of near-best strike–dip–rake solutions. The broad solution family (1,588 near-best mechanisms) quantifies the non-uniqueness produced by the sparse azimuthal sampling.

5.2 Two-dimensional Coulomb stress scenarios

At 10 km receiver depth, the NP1 scenario spans approximately −1.76 to +0.69 MPa over the full numerical grid, whereas NP2 spans approximately −1.66 to +1.96 MPa. These maxima occur in the strongly heterogeneous near-source field and should not be interpreted as regional stress levels. The 95th percentile of |ΔCFS| over the complete grids is only ~0.0016 MPa for NP1 and ~0.0013 MPa for NP2, demonstrating that the strongest extrema occupy a small fraction of the model domain.

Both scenarios contain alternating positive and negative lobes around the source, but the detailed geometry rotates and changes amplitude with the nodal plane. This is precisely why a single attractive Coulomb map can be misleading when the rupture plane is uncertain.

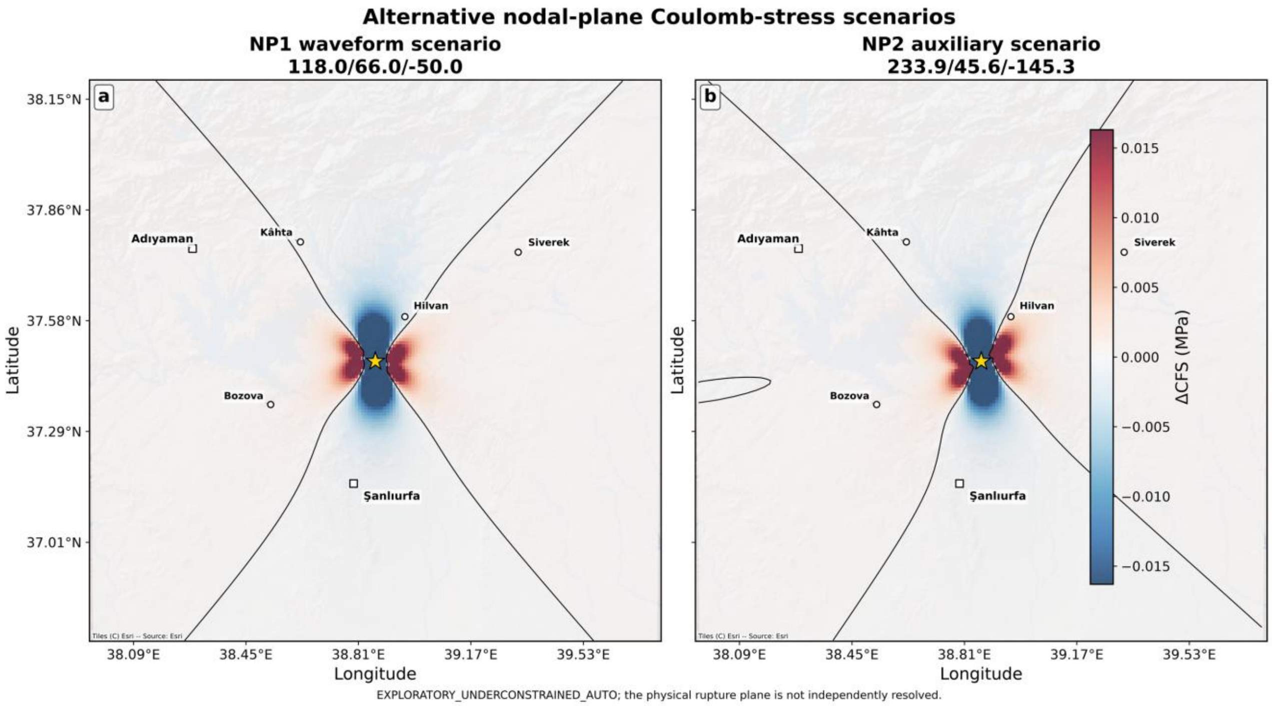

Figure 6. Alternative NP1 and NP2 Coulomb failure stress scenarios plotted on a common color scale and real basemap. Place names are redrawn above the stress raster for readability. The physical rupture plane remains unresolved.

5.3 Robust near-source monitoring sectors

The nodal-plane consensus analysis yields two compact robust-positive sectors after excluding the inner 5 km source core. The western sector has centroid approximately 37.4672°N, 38.7862°E, area ~34.0 km², radial extent ~5.2–10.4 km from the USGS epicenter, and maximum consensus stress ~+0.0498 MPa. The eastern sector has centroid approximately 37.4808°N, 38.9369°E, area ~34.0 km², radial extent ~5.2–9.9 km, and maximum consensus stress ~+0.0496 MPa. Because these values are the minimum of the two scenario stresses at each point, the sectors are more robust to nodal-plane ambiguity than either individual map.

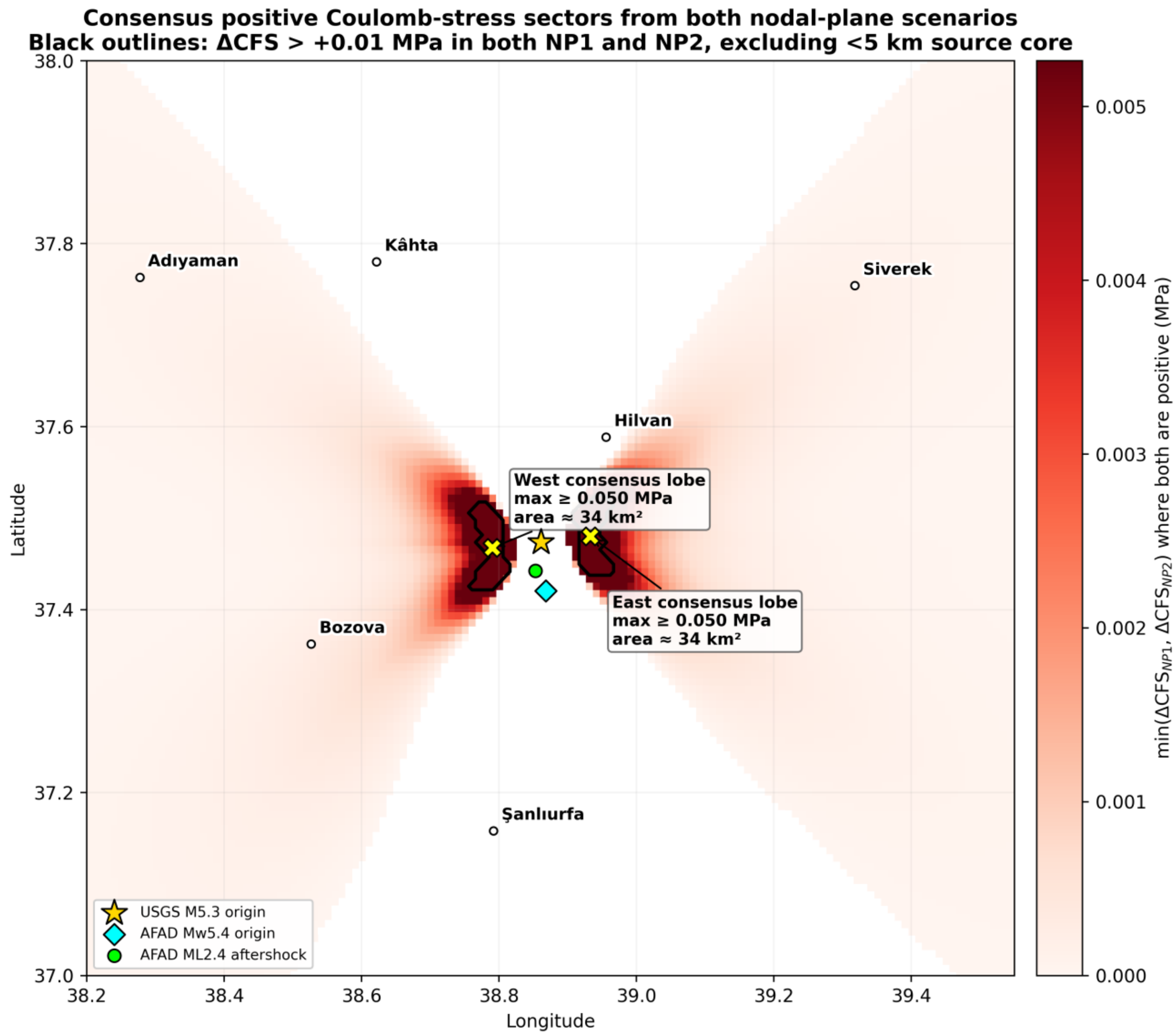

Figure 7. Nodal-plane-consensus static stress map used to define monitoring priorities. Black outlines delimit cells outside the 5 km source core for which both NP1 and NP2 exceed +0.01 MPa. The two compact east–west sectors are investigation targets, not predicted earthquake locations. USGS and AFAD rapid origins and the early AFAD ML 2.4 aftershock are shown for comparison.

Table 3. Model-based near-source investigation sectors.

Sector	Centroid lat.	Centroid lon.	Area km²	Radius km	Max consensus MPa	Monitoring priority
West consensus sector	37.4672	38.7862	~34.0	5.2–10.4	+0.0498	Highest
East consensus sector	37.4808	38.9369	~34.0	5.2–9.9	+0.0496	Highest
0–5 km source core	USGS epicentral area	—	—	0–5	Not used for screening	High, but model-sensitive

5.4 Stress values at named settlement centers

Interpolated stress at the centers of major nearby settlements is much smaller than the +0.01 MPa monitoring-screening reference. Hilvan itself is mixed-sign between the two scenarios. Bozova, Siverek and Adıyaman are positive in both scenarios but only at ~10^−4 MPa scale, roughly two orders of magnitude below the reference contour. These point calculations do not measure local building risk, site amplification, shaking intensity or stress on nearby mapped faults; they simply demonstrate that the strongest consensus static-stress feature in this model is near-source rather than centered on a major city.

Table 4. Modelled 10 km-depth ΔCFS at selected settlement centers.

Place	Distance km	NP1 MPa	NP2 MPa	Scenario agreement
Hilvan	15.2	−0.002341	+0.001805	Mixed sign
Şanlıurfa	35.5	−0.000757	−0.000449	Both negative
Siverek	50.9	+0.000125	+0.000140	Both positive, very small
Bozova	32.1	+0.000404	+0.000245	Both positive, very small
Kâhta	40.1	−0.000089	−0.000210	Both negative/near zero
Adıyaman	60.8	+0.000078	+0.000069	Both positive, very small

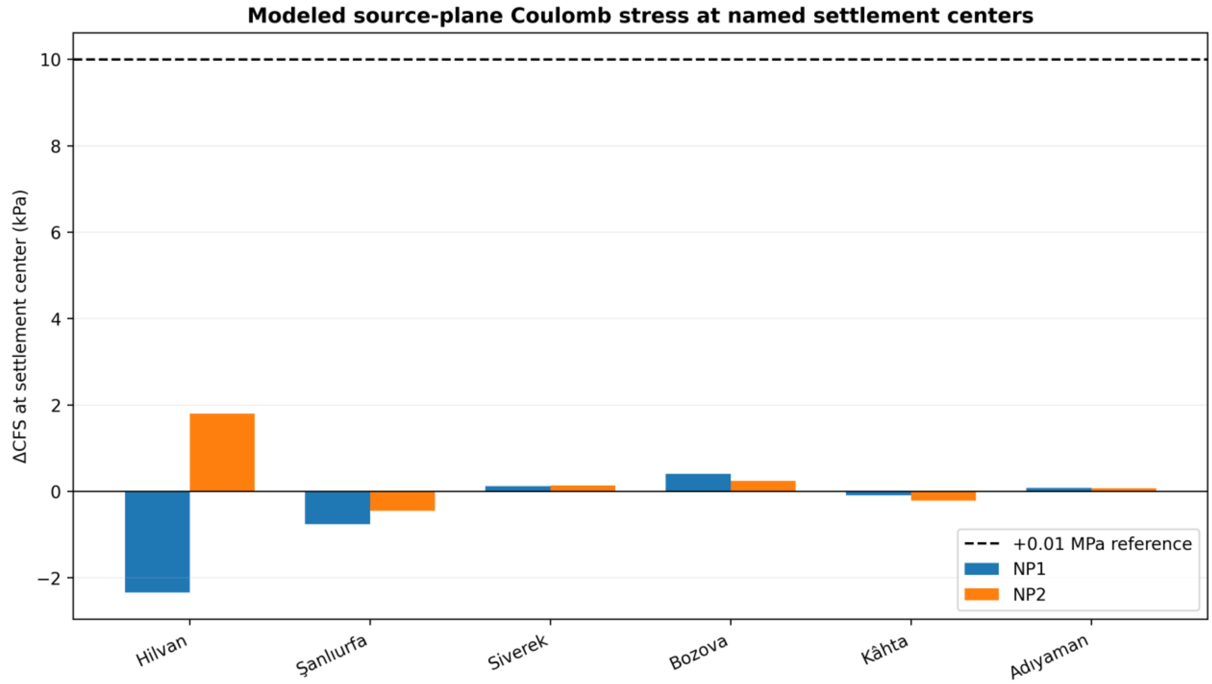

Figure 8. Modeled ΔCFS at selected settlement centers for NP1 and NP2 scenarios. Values are shown in kPa and compared with the +0.01 MPa (10 kPa) screening reference. This is not a ranking of urban seismic hazard.

5.5 Three-dimensional and depth-dependent stress structure

Recalculation on receiver planes at 2, 5, 10, 15 and 20 km depth shows a vertically concentrated stress perturbation. The 95th percentile |ΔCFS| remains of order 0.0016–0.0038 MPa across these slices, while local near-source extrema increase strongly near the modeled source depth. The broad positive-area fraction ranges from ~0.60 to 0.64, but area fraction alone is not a hazard metric because the majority of positive cells have very small amplitudes.

Table 5. NP1 depth-slice Coulomb stress summary from the supplementary workflow.

Depth km	Min MPa	Max MPa	95th |ΔCFS| MPa	Positive fraction
2	-0.0233	0.0191	0.0027	0.602
5	-0.0630	0.0724	0.0026	0.604
10	-1.9416	0.4549	0.0038	0.632
15	-0.0670	0.0698	0.0027	0.640
20	-0.0110	0.0103	0.0016	0.630

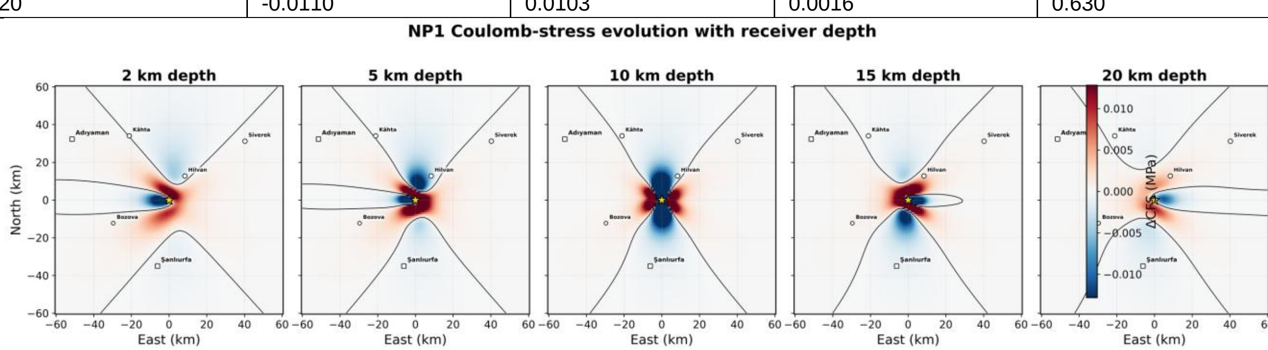

Figure 9. NP1 Coulomb stress slices at 2, 5, 10, 15 and 20 km receiver depth. The source-depth slice contains the strongest localized gradients.

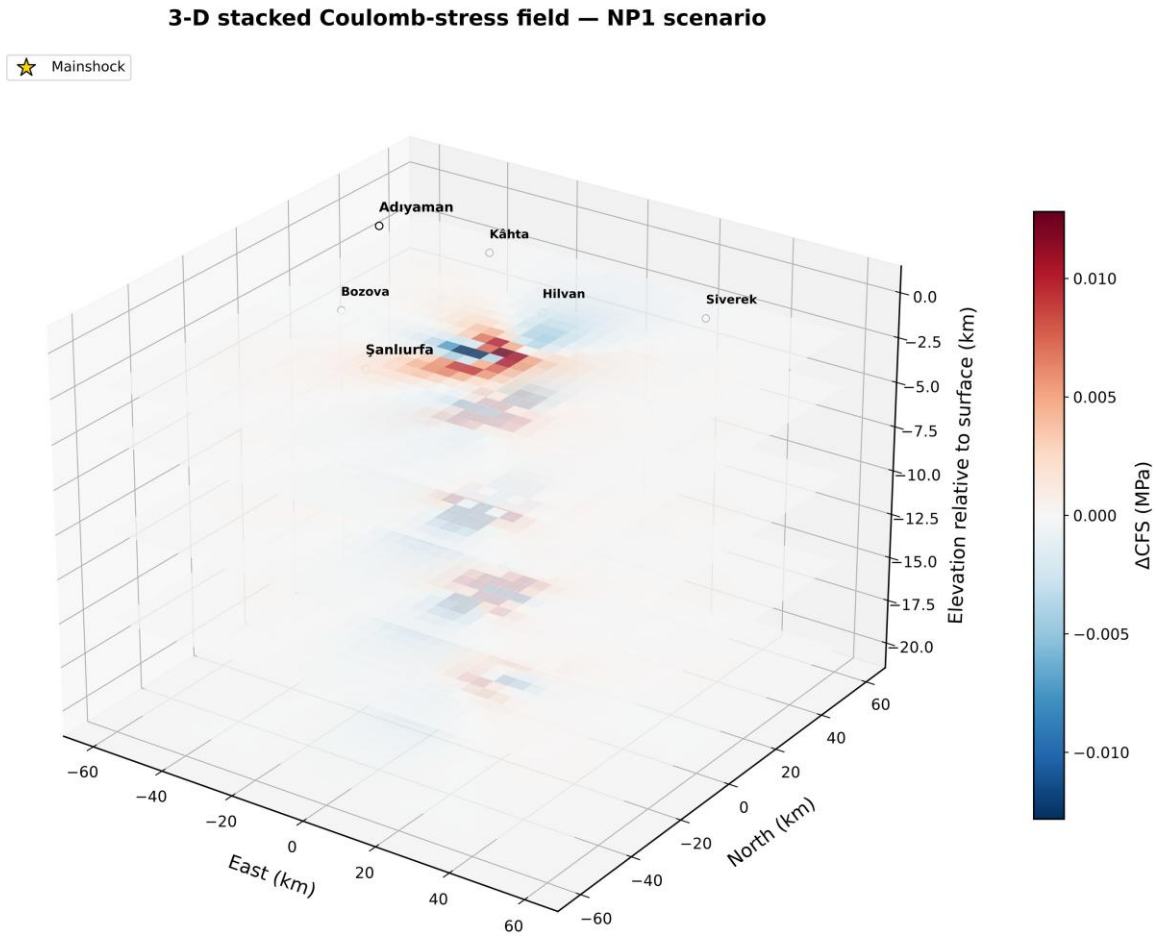

Figure 10. Three-dimensional stack of NP1 Coulomb stress slices. The visualization emphasizes the depth localization and lobe geometry of the elastic model.

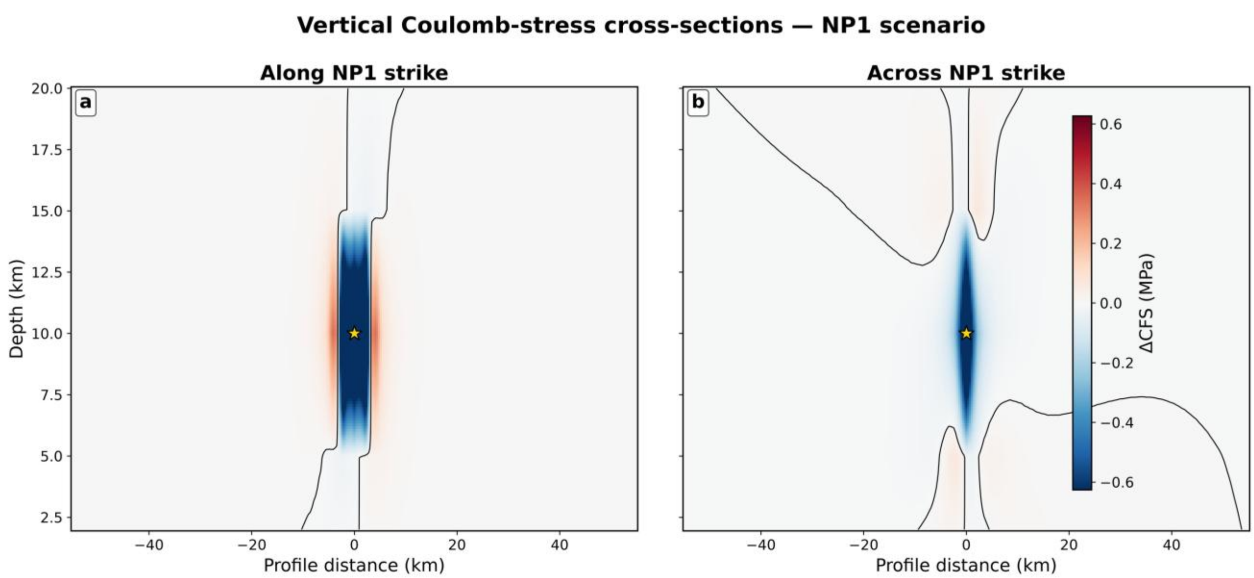

Figure 11. Along-strike and across-strike vertical Coulomb stress sections through the NP1 source scenario.

5.6 Macroseismic evidence from USGS DYFI

The same-day DYFI product provides an independent qualitative check that the earthquake produced clearly perceptible shaking. The USGS DYFI list displayed community intensity V from 8 responses. Intensity V is consistent with a moderate felt event, but the small number of reports means that this value should be treated as a preliminary community-level observation rather than a dense macroseismic field. In particular, the available DYFI information does not resolve the east–west Coulomb-stress lobes, does not identify the rupture plane, and does not provide evidence that any particular settlement is the next likely rupture location.

The main value of the DYFI update for this rapid study is therefore complementary: the waveform analysis constrains source kinematics and the elastic model tests stress-transfer hypotheses, whereas DYFI documents human-perceived shaking. Keeping these evidence streams separate avoids conflating felt intensity with static stress change.

6. Discussion

6.1 What can—and cannot—be inferred from the rapid focal mechanism

The first-motion inversion successfully converts the downloaded waveforms into a testable source hypothesis, but it also demonstrates why fit quality alone is an insufficient measure of solution reliability. Five polarities can be fit exactly by many double-couple mechanisms when the azimuth gap exceeds 180°. Hardebeck and Shearer (2002) showed that focal mechanisms should be evaluated as families that reflect location, velocity-model and polarity uncertainties, and SKHASH formalizes this approach with weighted observations and randomized source/velocity perturbations (Skoumal et al., 2024). The present grid-search result should therefore be treated as a provisional member of an oblique-faulting family pending additional first motions and regional waveform moment-tensor inversion.

A practical next step is to extend the source inversion beyond first motions. The dataset contains three-component waveforms suitable, after rigorous response and timing checks, for regional moment-tensor fitting using Green's functions and a southeastern Türkiye velocity model. Such an inversion could constrain centroid depth, double-couple percentage and the orientation of both nodal planes more strongly than the current five-polarity solution.

6.2 Hypocentral uncertainty is comparable to the stress-lobe scale

The USGS and AFAD rapid epicenters differ by ~5.9 km. The two robust-positive consensus sectors begin at ~5.2 km from the USGS epicenter and have centroids ~6–7 km from it. Consequently, shifting the source to the AFAD rapid location could move the inferred monitoring sectors by an amount comparable to their distance from the source. This is one of the strongest reasons not to name a specific village, road corridor or fault patch as the expected site of a future earthquake from the present calculation.

Rapid double-difference relocation of the mainshock and aftershocks should therefore precede any operational fault-specific CFS interpretation. The relocation should use a local velocity model, station corrections and, where possible, waveform cross-correlation. The stress model should then be recomputed around the relocated source.

6.3 The early aftershock is a useful falsification test

An early AFAD ML 2.4 event at approximately 37.44233°N, 38.853°E and 11.3 km depth provides a useful caution. When sampled on the present 10 km source-plane receiver grids centered on the USGS source, its location falls in negative ΔCFS in both alternative scenarios (approximately −0.18 MPa for NP1 and −0.52 MPa for NP2). This does not invalidate Coulomb physics; it invalidates the simplistic interpretation that the current source-plane CFS map should predict every early aftershock.

Aftershocks occur on faults with their own orientations, frictional states, pore pressures and pre-mainshock stresses. A receiver plane aligned with the source plane may be inappropriate for an aftershock on a differently oriented fault. Moreover, the sampled point is close to the source where rapid-catalog location differences and idealized rectangular slip geometry strongly affect the calculated tensor. This observation should be treated as an explicit model-checking constraint in subsequent work.

6.4 Relationship to the local fault and reservoir system

The earthquake lies in a region where the Bozova–Samsat–Kalecik fault system and the Atatürk Reservoir have previously been studied for moderate seismicity and effective-stress changes (Büyükakpınar et al., 2021). However, the present rapid source solution does not contain a digital active-fault intersection test and does not establish that either consensus lobe lies on one of these mapped faults. Geological assignment should therefore wait for accurate hypocentral relocation, focal-mechanism validation and an authoritative active-fault GIS layer.

Similarly, no reservoir-triggering claim is made. Demonstrating reservoir influence requires temporal reservoir-level data, poroelastic/hydraulic modelling, background-rate analysis, hypocentral depth constraints and comparison with tectonic loading. The prior Atatürk Reservoir literature makes this a worthwhile research question, not a conclusion.

6.5 Monitoring priorities for the next hours to weeks

The present model can support prioritization of observations even though it cannot forecast the next earthquake. The most defensible priorities are organized by robustness rather than by population center.

- Priority A — Near-source east and west consensus-positive sectors: deploy temporary short-period/broadband stations within ~20 km of the source, with particular density across the two 5–10 km consensus lobes. The objective is to detect microseismic migration, improve relative locations and determine whether activity aligns with a specific fault.
- Priority A — Rapid geodesy: process the first available Sentinel-1 InSAR pair and any continuous/high-rate GNSS data. Even small surface deformation can help select between nodal planes and constrain centroid depth and rupture dimensions.
- Priority A — Receiver-fault characterization: compile MTA/EDSF/local fault traces and compute ΔCFS separately on each plausible fault orientation rather than on the source plane alone.
- Priority B — Atatürk Reservoir structural corridor: monitor the local Bozova–Samsat–Kalecik system and reservoir margins because of the established history of shallow moderate seismicity, but do not interpret this priority as evidence that the 2026 event was reservoir triggered.
- Priority B — Hilvan–Karaköprü near-source area: maintain enhanced seismic and engineering observations because of proximity to the hypocentral uncertainty envelope, not because the town centers are predicted to host the next rupture.
- Priority C — Şanlıurfa, Siverek, Bozova, Kâhta and Adıyaman: continue normal regional seismic surveillance and post-shaking structural inspections as appropriate. The current point-sampled CFS model does not support ranking any of these settlement centers as a likely 'next earthquake' location.

Operational interpretation rule
Monitoring priority ≠ earthquake forecast.
Positive ΔCFS means increased modeled tendency to fail only on the specified receiver geometry and under the assumed elastic/frictional model.
No statement in this manuscript assigns a probability, time window, or magnitude to a future earthquake.

6.6 Relevance to recent southeastern Türkiye stress-transfer studies

Stress-transfer analyses of the 2023 Kahramanmaraş sequence demonstrate that coseismic stress perturbations can interact with inherited tectonic loading and multiple fault geometries (Nalbant et al., 2026). The scale and data richness of that sequence are very different from the present M5-class event, but the conceptual lesson is relevant: stress changes should be evaluated on realistic fault systems and in the context of pre-existing loading. The current Hilvan–Karaköprü model is therefore best regarded as a rapid initial condition for more complete fault-network modelling.

6.7 Macroseismic observations and implications for field follow-up

The USGS DYFI update strengthens the case for targeted post-event field documentation, but it does not alter the physical Coulomb-stress interpretation. With only eight same-day reports, the current macroseismic sample is too sparse to distinguish local site amplification, building vulnerability, or detailed intensity decay between Hilvan, Karaköprü, Şanlıurfa and surrounding settlements. A structured field questionnaire and building-condition survey would therefore be scientifically useful, particularly if tied to geocoded locations and construction typology.

The temporal accumulation of DYFI reports should also not be compared directly with aftershock occurrence. Reporting rate depends on internet access, time of day, public awareness, media coverage, and delayed submissions. Accordingly, the DYFI responses-versus-time curve is best treated as metadata describing the growth of the citizen-observation sample during the first 24 h.

7. Limitations and uncertainty budget

I. Focal-mechanism geometry: only five weighted P polarities are used, including two lower-confidence fallback observations; the azimuth gap is 207.7°.

II. Mechanism non-uniqueness: 1,588 near-best solutions remain, so the preferred NP1/NP2 pair is not a tightly constrained source solution.

III. Velocity model: iasp91 is a global 1-D model. A local southeastern Türkiye crustal model would improve P takeoff angles and relative arrival predictions.

IV. Hypocenter: USGS and AFAD rapid locations differ by ~5.9 km and depths by ~3 km; both differences materially influence the near-source stress field.

V. Magnitude and source scaling: Mw 5.3 is used as a working magnitude proxy, with an assumed 3 MPa stress drop and uniform rectangular slip. No spectral stress-drop or finite-fault inversion is used.

VI. Receiver geometry: each Coulomb scenario resolves stress on a receiver plane with the same orientation as its source nodal plane. Real faults may have substantially different orientations.

VII. Elastic structure: the Okada model assumes a homogeneous isotropic half-space and does not incorporate layered elastic structure, topography, dynamic stress, poroelastic diffusion, viscoelasticity or fault-zone rheology (Toda et al., 2011).

VIII. Near-source singularity/sensitivity: stress extrema within and adjacent to the rectangular dislocation are highly sensitive to geometry and discretization; the consensus screening excludes the inner 5 km.

IX. Aftershock completeness: the same-day sequence is incomplete and rapidly evolving. Any comparison with early aftershocks is provisional.

X. Basemap/fault association: place-name maps improve geographic readability but do not constitute a validated active-fault assignment.

8. Conclusions

1. The 24 September 2026 Şanlıurfa (Karaköprü–Hilvan) earthquake was rapidly characterized using open waveform and station metadata within hours of origin time.
2. The waveform archive supports an exploratory first-motion mechanism, but the present five-polarity solution is underconstrained despite zero polarity misfit. The preferred nodal planes are NP1 = 118°/66°/−50° and NP2 = 233.9°/45.6°/−145.3°, with 1,588 near-best alternatives.
3. Alternative NP1/NP2 Okada models produce localized static stress changes around a magnitude-scaled rectangular source. A conservative nodal-plane-consensus filter identifies two ~34 km² sectors roughly 5–10 km west and east of the USGS epicenter where both scenarios exceed +0.01 MPa.
4. These two near-source sectors are the strongest current targets for dense seismic, geodetic and geological investigation. They are not predicted locations of the next earthquake.
5. Modeled ΔCFS at the centers of Hilvan, Şanlıurfa, Siverek, Bozova, Kâhta and Adıyaman is much smaller than the consensus screening reference; the present model does not justify ranking one of these cities as a future rupture site.
6. The ~5.9 km USGS–AFAD location difference is comparable to the lobe distance and must be reduced through rapid relocation before fault-specific stress interpretation.
7. The early ML 2.4 aftershock falls in negative ΔCFS under the source-plane receiver assumptions, demonstrating that receiver orientation and source uncertainty are essential. Future work should use a regional moment tensor, relocated seismicity, mapped receiver faults, InSAR/GNSS and sensitivity ensembles.

8. Same-day USGS DYFI observations reached 8 reports and community intensity V. These data provide useful macroseismic context but are still too sparse and dynamic to support spatial hazard ranking or stress-transfer inference.

9. Data and code availability

The rapid analysis used openly accessible waveform/station services and a local reproducibility archive containing the downloaded MiniSEED/SAC data, StationXML metadata, station geometry, focal-mechanism tables, Coulomb grids, and Jupyter notebooks. Before journal submission, the final frozen analysis package deposited in a persistent repository (10.5281/zenodo.22945868.) and the DOI inserted here. The current USGS event identifier is us6000tx9u. AFAD and KOERI data products should be cited according to their provider terms.

10. Author contributions

Shaheen Mohammed Saleh Ahmed: Conceptualization; Methodology; Software; Formal analysis; Investigation; Data curation; Visualization; Writing—original draft; Writing—review and editing. Confirm and revise the CRediT statement if additional authors contribute before submission.

11. Funding

No external funding was declared for this rapid-response analysis. Replace this statement if funding or institutional support applies.

12. Competing interests

The author declares no competing interests related to this study.

13. Acknowledgements

The author acknowledges the seismic network operators and FDSN data centers that make real-time and near-real-time waveform and metadata access possible, including USGS, KOERI and other participating providers. AFAD and USGS rapid earthquake solutions were used for first-hours comparison. The computational workflow uses open-source scientific Python tools and an Okada elastic-dislocation implementation.

References

AFAD (Disaster and Emergency Management Authority of Türkiye). (2026). Son Depremler / Last Earthquakes. Rapid catalogue entry for the 24 September 2026 Şanlıurfa earthquake. Accessed 24 September 2026.

Beyreuther, M., Barsch, R., Krischer, L., Megies, T., Behr, Y., & Wassermann, J. (2010). ObsPy: A Python toolbox for seismology. Seismological Research Letters, 81(3), 530–533. https://doi.org/10.1785/gssrl.81.3.530

Büyükakpınar, P., Cesca, S., Hainzl, S., Jamalreyhani, M., Heimann, S., & Dahm, T. (2021). Reservoir-triggered earthquakes around the Atatürk Dam (southeastern Turkey). Frontiers in Earth Science, 9, 663385. https://doi.org/10.3389/feart.2021.663385

Cheloni, D., & Akinci, A. (2020). Source modelling and strong ground motion simulations for the 24 January 2020, Mw 6.8 Elazığ earthquake, Turkey. Geophysical Journal International, 223(2), 1054–1068. https://doi.org/10.1093/gji/ggaa350

Duman, T. Y., & Emre, Ö. (2013). The East Anatolian Fault: geometry, segmentation and jog characteristics. Geological Society, London, Special Publications, 372(1), 495–529. https://doi.org/10.1144/SP372.14

Güvercin, S. E., Karabulut, H., Konca, A. Ö., Doğan, U., & Ergintav, S. (2022). Active seismotectonics of the East Anatolian Fault. Geophysical Journal International, 230(1), 50–69. https://doi.org/10.1093/gji/ggac045

Hardebeck, J. L., & Shearer, P. M. (2002). A new method for determining first-motion focal mechanisms. Bulletin of the Seismological Society of America, 92(6), 2264–2276. https://doi.org/10.1785/0120010200

Kennett, B. L. N., & Engdahl, E. R. (1991). Traveltimes for global earthquake location and phase identification. Geophysical Journal International, 105(2), 429–465. https://doi.org/10.1111/j.1365-246X.1991.tb06724.x

King, G. C. P., Stein, R. S., & Lin, J. (1994). Static stress changes and the triggering of earthquakes. Bulletin of the Seismological Society of America, 84(3), 935–953. https://doi.org/10.1785/BSSA0840030935

Konca, A. Ö., Karabulut, H., Güvercin, S. E., et al. (2021). From interseismic deformation with near-repeating earthquakes to co-seismic rupture: A unified view of the 2020 Mw 6.8 Sivrice (Elazığ) Eastern Turkey earthquake. Journal of Geophysical Research: Solid Earth, 126, e2021JB021830. https://doi.org/10.1029/2021JB021830

McClusky, S., Balassanian, S., Barka, A., et al. (2000). Global Positioning System constraints on plate kinematics and dynamics in the eastern Mediterranean and Caucasus. Journal of Geophysical Research: Solid Earth, 105(B3), 5695–5719. https://doi.org/10.1029/1999JB900351

Nalbant, S. S., Uzunca, F., Main, I. G., Utkucu, M., et al. (2026). Stress-mediated multi-fault rupture dynamics of the 2023 Kahramanmaraş earthquake sequence, Türkiye. Scientific Reports, 16, 10705. https://doi.org/10.1038/s41598-026-45723-7

Okada, Y. (1992). Internal deformation due to shear and tensile faults in a half-space. Bulletin of the Seismological Society of America, 82(2), 1018–1040. https://doi.org/10.1785/BSSA0820021018

Reilinger, R., McClusky, S., Vernant, P., et al. (2006). GPS constraints on continental deformation in the Africa–Arabia–Eurasia continental collision zone and implications for the dynamics of plate interactions. Journal of Geophysical Research: Solid Earth, 111, B05411. https://doi.org/10.1029/2005JB004051

Skoumal, R. J., Hardebeck, J. L., & Shearer, P. M. (2024). SKHASH: A Python package for computing earthquake focal mechanisms. Seismological Research Letters, 95(4), 2519–2526. https://doi.org/10.1785/0220230329

Toda, S., Stein, R. S., Richards-Dinger, K., & Bozkurt, S. B. (2005). Forecasting the evolution of seismicity in southern California: Animations built on earthquake stress transfer. Journal of Geophysical Research: Solid Earth, 110, B05S16. https://doi.org/10.1029/2004JB003415

Toda, S., Stein, R. S., Sevilgen, V., & Lin, J. (2011). Coulomb 3.3 graphic-rich deformation and stress-change software for earthquake, tectonic, and volcano research and teaching—User guide. U.S. Geological Survey Open-File Report 2011–1060. https://doi.org/10.3133/ofr20111060

U.S. Geological Survey. (2026). M 5.3 — 15 km SSW of Hilvan, Turkey; event us6000tx9u, 24 September 2026. USGS Earthquake Hazards Program. Accessed 24 September 2026.

U.S. Geological Survey. (2026). Did You Feel It? Scientific background. Earthquake Hazards Program. Accessed 24 September 2026.

U.S. Geological Survey. (2026). Did You Feel It? responses-versus-time product for event us6000tx9u, M 5.3 — 15 km SSW of Hilvan, Turkey. Earthquake Hazards Program. Accessed 24 September 2026.

Supplementary Figures

These supplementary visualizations are included in the manuscript draft because the rapid analysis is strongly dependent on source geometry and uncertainty. For journal submission, the editor may request that some panels be moved to a separate Supplementary Information file.

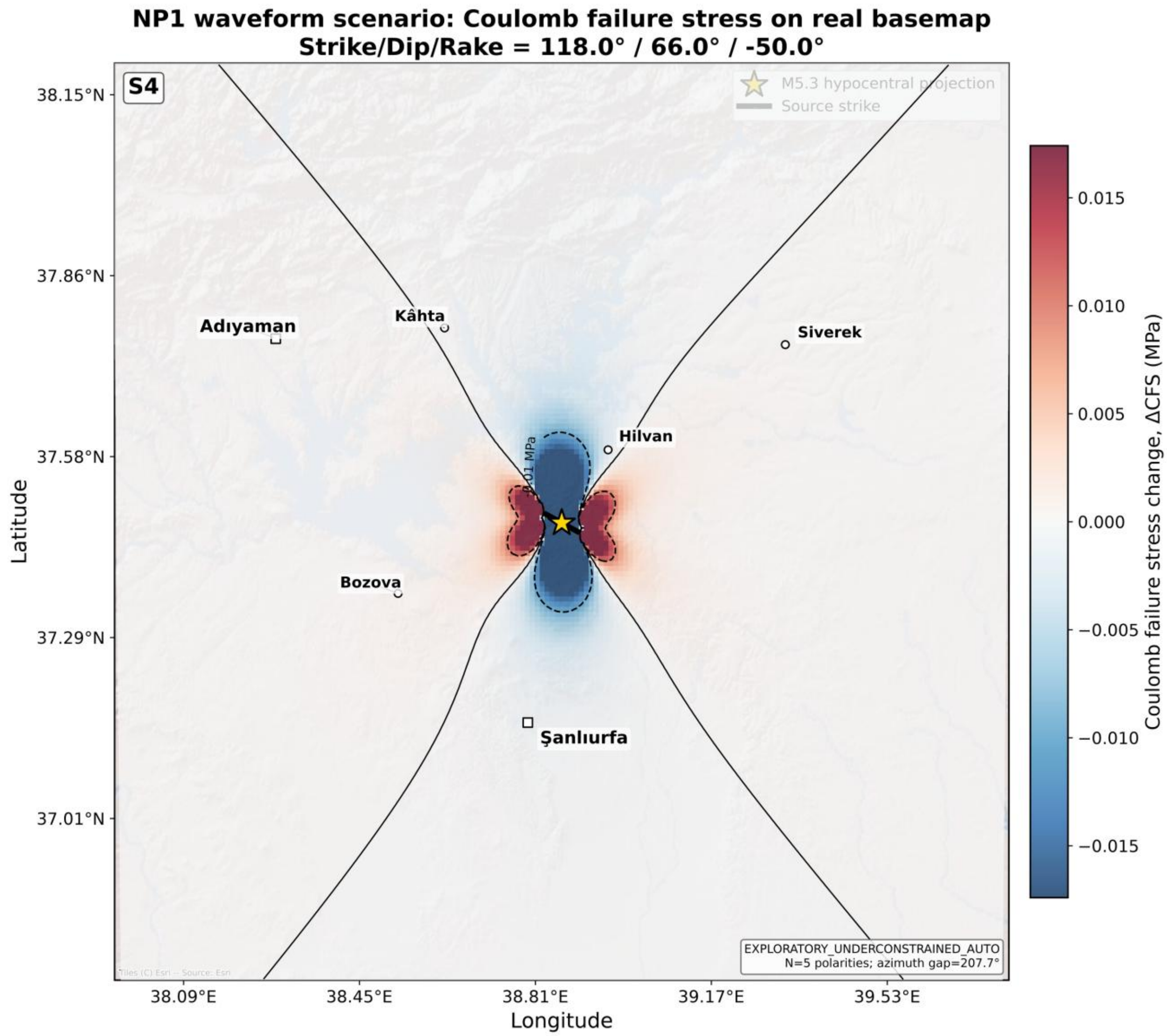

Figure S1. NP1 Coulomb failure stress at the parent receiver depth on a real basemap, with geographic place labels redrawn above the stress raster.

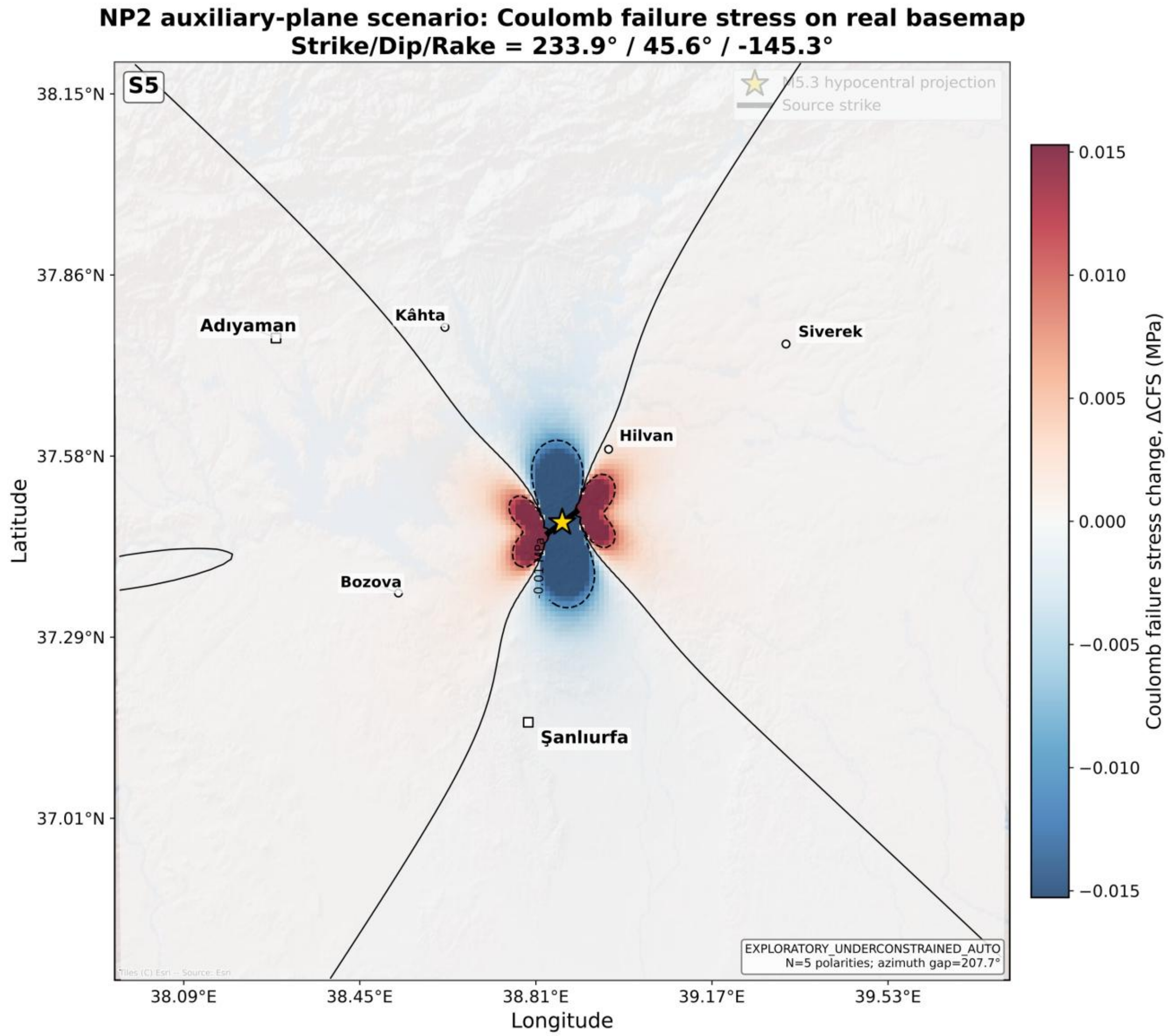

Figure S2. NP2 auxiliary-plane Coulomb failure stress at the parent receiver depth on a real basemap.

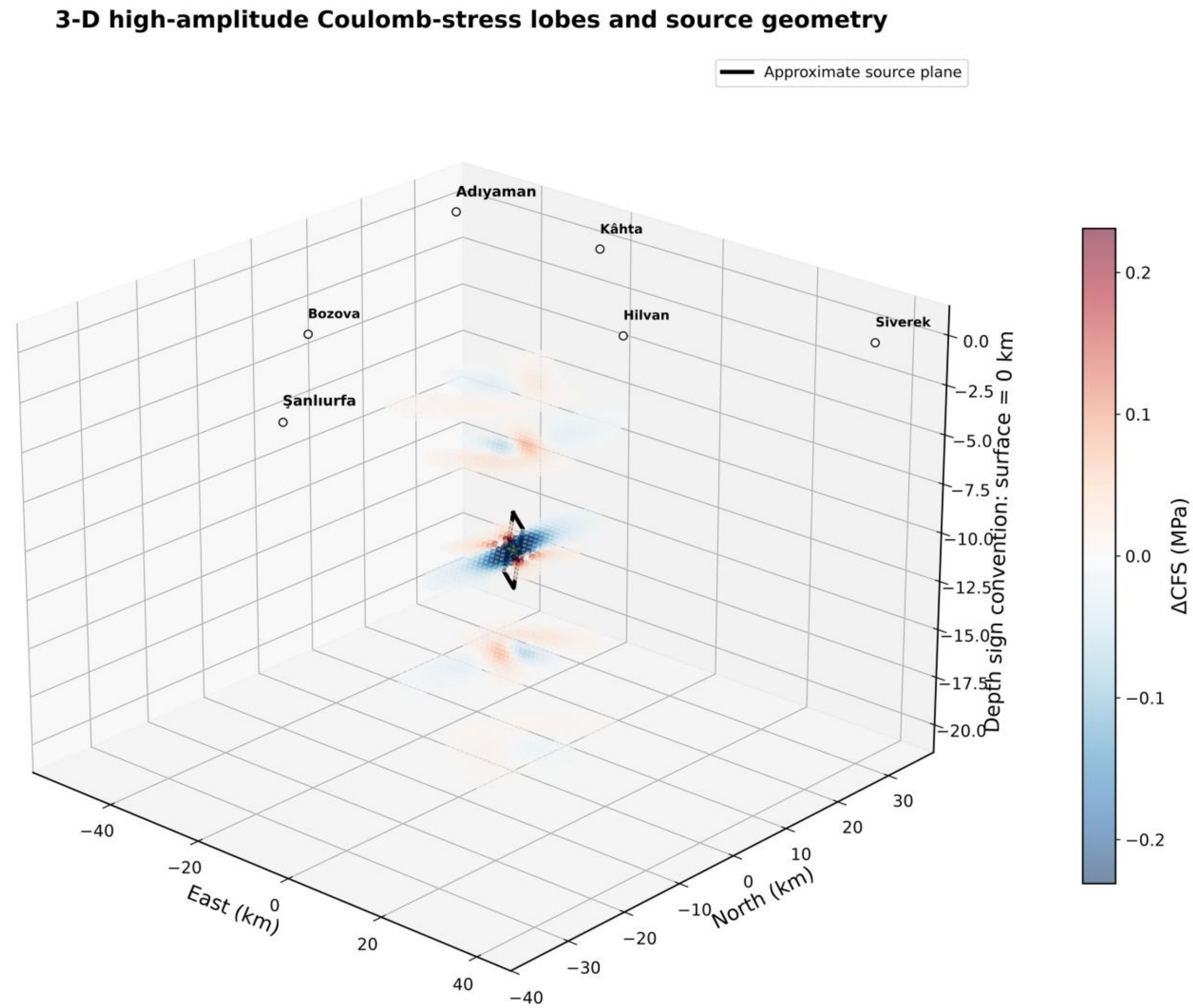

Figure S3. Three-dimensional high-amplitude Coulomb lobes and approximate rectangular source plane. This is a visualization of the elastic model, not a 3-D inversion.

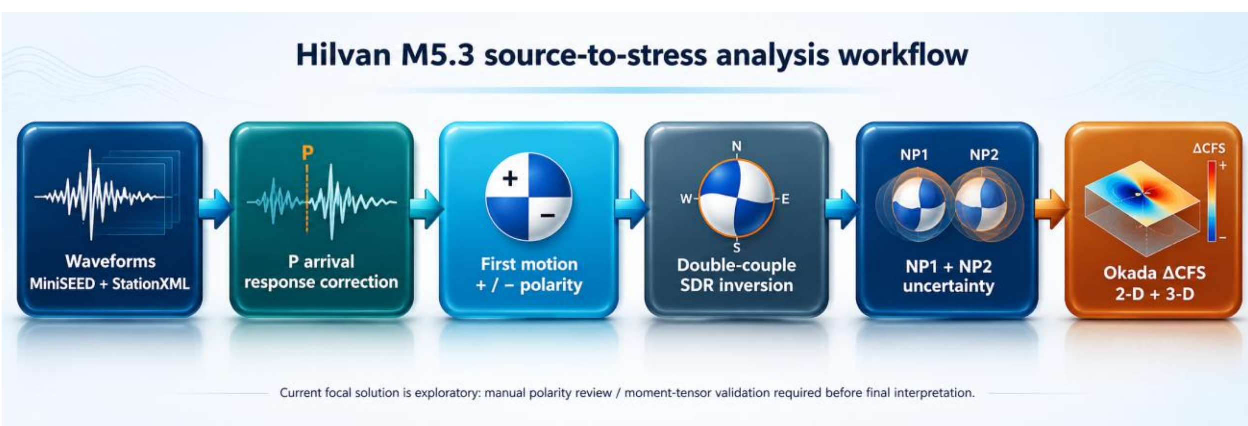

Figure S4. Rapid waveform-to-stress workflow from downloaded MiniSEED/StationXML data through P first-motion inversion and alternative NP1/NP2 Coulomb calculations.

Mechanism and Coulomb-model quality-control summary

Diagnostic	Current result	Publication expectation	Assessment
Number of polarities	5	Target ≥8–12 well-distributed observations	Needs improvement
Maximum azimuth gap	207.7°	Prefer <180°, ideally substantially smaller	Needs improvement
Polarity fit	0/5 parent misfit	Low misfit is desirable	Good fit but non-unique
Near-best solutions	1588	Fewer/narrower families indicate stronger constraint	Highly non-unique
Instrument response	StationXML corrected in parent	Required for consistent waveform polarity/amplitude	Implemented
Nodal-plane identity	NP1 and NP2 retained	Independent geological/geodetic constraint required	Unresolved
Finite source	Mw/stress-drop scaled rectang	Finite-fault/geodetic source preferred	Exploratory assumption
Coulomb sensitivity	Optional in parent notebook	Stress drop, friction, depth, receiver orientation should be tested	Recommended before paper

Figure S5. Graphical quality-control summary emphasizing the strengths and limitations of the current mechanism and Coulomb model.

Supplementary Table S1. Numerical stress-transfer screening values

Feature	Latitude	Longitude	Model value	Interpretation
West consensus sector	37.4672	38.7862	+0.0498 MPa	Both NP1 and NP2 > +0.01 MPa outside 5 km core
East consensus sector	37.4808	38.9369	+0.0496 MPa	Both NP1 and NP2 > +0.01 MPa outside 5 km core
AFAD rapid mainshock location	37.4205	38.86783	NP1 −0.1285; NP2 −0.1213 MPa	Shows sensitivity to source-location difference
Early AFAD ML2.4 aftershock	37.44233	38.853	NP1 −0.1812; NP2 −0.5203 MPa	Negative in source-plane receiver scenarios; not a predictor failure test

DYFI revision note: immediately before submission, re-check the USGS DYFI page because response counts and community intensity products may continue to evolve.